Supplementary Information for

Atypical Breathing Driven Two-Dimensional Valley Multiferroicity

Yangyang Feng, Jiangyu Zhao, Ying Dai,* Baibiao Huang, Yandong Ma*

School of Physics, State Key Laboratory of Crystal Materials, Shandong University, Shandanan Street 27, Jinan 250100, China

*Corresponding author: daiy60@sdu.edu.cn (Y.D.); yandong.ma@sdu.edu.cn (Y.M.)

Tight-binding model

To describe the valley physics of the lattice, we construct an effective tight-binding model for characterizing the low-energy band dispersions around the Fermi level.

$$H = -t\sum_{<i,j>} c_i^{\dagger}c_j + i\lambda_{SOC}\sum_{<<i,j>>} \upsilon_{ij}c_i^{\dagger}s_z c_j + m\sum_i \sigma_z c_i^{\dagger}s_z c_i + U\sum_i \delta c_i^{\dagger}c_i + h.c. \tag{1}$$

Here, $c_i^{\dagger}$ (c_i) is the creation (annihilation) operator of an electron on site *i*. The first term represents nearest-neighbor (NN) hopping with transfer energy *t*, and could also be considered as inter-sublattice interaction. The second term indicates the next-nearest-neighbor (NNN) SOC with λ_{SOC} denoting the strengths. $\upsilon_{ij} = \pm 1$ corresponds to the counterclockwise/clockwise hopping. The third term describes antiferromagnetic exchange interaction with spontaneous magnetic moment: $m = <n_{i,\uparrow}\text{-}n_{i,\downarrow}>$. *U* represents the effect of out-of-plane electric polarization. $\delta = \pm 1$ corresponds to the A- and B-sublattices. $\boldsymbol{\sigma}_z$ and $\boldsymbol{s}_z$ are the Pauli matrices for the isospin and spin degrees of freedom, respectively.

According to **Fig. 2(a)**, the NN and NNN basis vectors are respectively written as

$$a_1 = (0,1)\ \ a_2 = (-\frac{\sqrt{3}}{2}, -\frac{1}{2})\ \ a_3 = (\frac{\sqrt{3}}{2}, -\frac{1}{2}) \tag{2}$$

$$b_1 = (\sqrt{3}, 0)\ \ b_2 = (-\frac{\sqrt{3}}{2}, \frac{3}{2})\ \ b_3 = (-\frac{\sqrt{3}}{2}, -\frac{3}{2}) \tag{3}$$

After Fourier transformation, the Eq. (1) is transferred into momentum space, and the four terms can be given as

$$\begin{pmatrix} 0 & -t(e^{-ik\cdot a_1} + e^{-ik\cdot a_2} + e^{-ik\cdot a_3}) \\ -t(e^{ik\cdot a_1} + e^{ik\cdot a_2} + e^{ik\cdot a_3}) & 0 \end{pmatrix} \otimes \boldsymbol{\sigma_0} \otimes \boldsymbol{s_0} \tag{4}$$

$$\begin{pmatrix} [i\lambda_{SOC}\upsilon_A(e^{-ik\cdot b_1} + e^{-ik\cdot b_2} + e^{-ik\cdot b_3}) + h.c.] \otimes \boldsymbol{s}_z & 0 \otimes \boldsymbol{s}_0 \\ 0 \otimes \boldsymbol{s}_0 & [i\lambda_{SOC}\upsilon_B(e^{-ik\cdot b_1} + e^{-ik\cdot b_2} + e^{-ik\cdot b_3}) + h.c.] \otimes \boldsymbol{s}_z \end{pmatrix} \otimes \boldsymbol{\sigma_0} \tag{5}$$

$$\begin{pmatrix} m & 0 \\ 0 & m \end{pmatrix} \otimes \boldsymbol{\sigma}_z \otimes \boldsymbol{s}_z \tag{6}$$

$$\begin{pmatrix} U & 0 \\ 0 & -U \end{pmatrix} \otimes \boldsymbol{\sigma}_0 \otimes \boldsymbol{s}_0 \tag{7}$$

Considering the Néel-type AFM coupling of the system, we employ a simplified four-band model by focusing on a single spin channel within each sublattice (spin-down channel of A-sublattice and spin-up channel of B-sublattice). In this case, the low-energy effective Hamiltonian can be expressed as

$$H = \begin{pmatrix} -2\lambda_{SOC}\upsilon_A\gamma(k)\sigma_0 + m\sigma_z + U\sigma_0 & -tf(k)\sigma_0 \\ -tf^*(k)\sigma_0 & 2\lambda_{SOC}\upsilon_B\gamma(k)\sigma_0 - m\sigma_z - U\sigma_0 \end{pmatrix} \quad (8)$$

Here, $\gamma(k) = \sin(\sqrt{3}k_y) - 2\cos(\frac{3}{2}k_x)\sin(\frac{\sqrt{3}}{2}k_y)$ and $f(k) = e^{-ik_x} + 2e^{\frac{ik_y}{2}}\cos(\frac{\sqrt{3}}{2}k_y)$. Due to the atypical lattice breathing during the ferroelectric transition as defined in main text, the υ_A and υ_B related to phase of NNN hopping have same or different values under state-I, state-II and state-PE. The details of the specific values are listed in **Table S1**.

Table S1. The tight-binding model parameters υ_A and υ_B under state-I, state-II and state-PE.

	υ_A	υ_B
State-I	+1	+1
State-PE	-1	+1
State-II	-1	-1

Table S2. The tight-binding model parameters for the band dispersions and Berry curvature near the Fermi level. All the parameters are in units of eV.

t	$\boldsymbol{\lambda_{soc}}$	***m***	***U***
0.4	0.01	0.5	0.2

Table S3. Lattice constants (a, b) and axial angle (α, β, γ) under state-I, state-AFE, state-PE, and state-II for SL Gd_2CO_2.

	a **(Å)**	***b*** **(Å)**	**α (°)**	**β (°)**	**γ (°)**
State-I/II	3.796	3.796	90.0	90.0	120.0
State-AFE	7.465	7.433	90.1	90.9	119.9
State-PE	3.721	3.721	90.0	90.0	120.0

Table S4. The energy difference of four possible magnetic orders: ferromagnetic (FM), stripy-type antiferromagnetic (sAFM), Néel-type antiferromagnetic (nAFM), and zigzag-type antiferromagnetic (zAFM).

	FM	**sAFM**	**nAFM**	**zAFM**
ΔE (meV)	0	-5.67	-4.99	-11.04

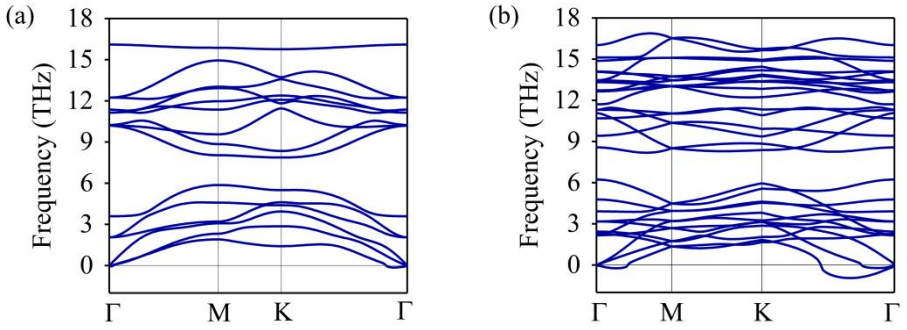

Fig. S1 Phonon spectra for (a) SL Gd_2CO_2 and (b) strained Gd_2CO_2.

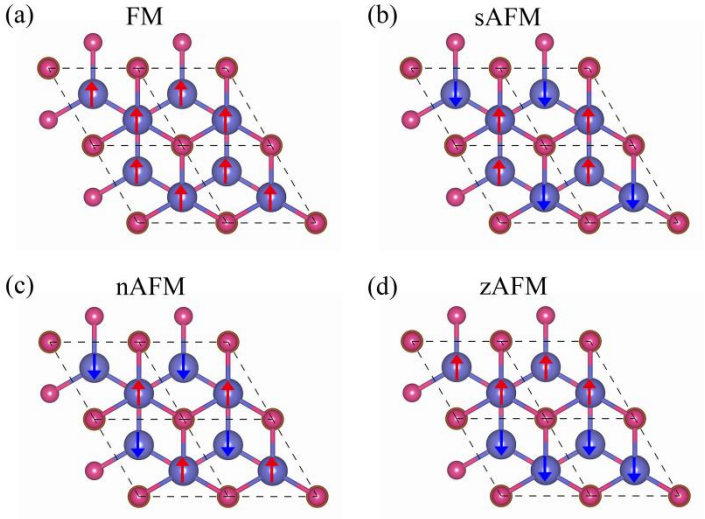

Fig. S2 Schematic diagrams of four possible magnetic orders: (a) FM, (b) sAFM, (c) nAFM, and (d) zAFM.

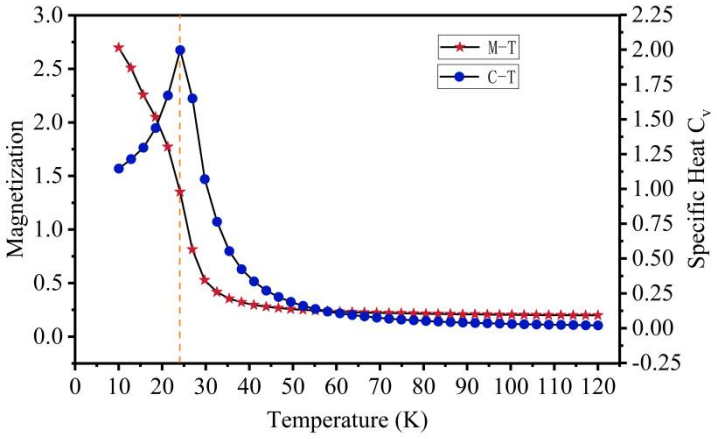

Fig. S3 Magnetization and specific heat C_V as a function of temperature for SL Gd_2CO_2.

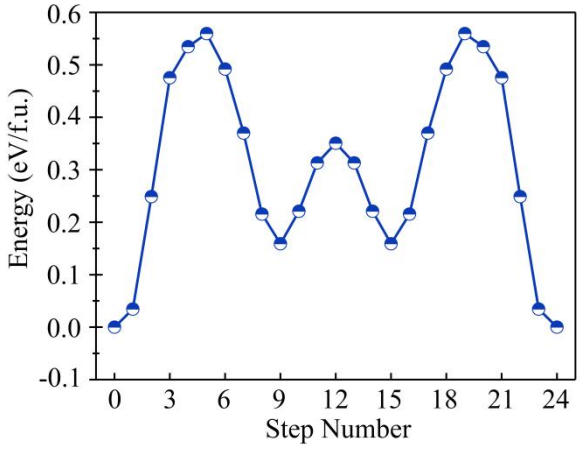

Fig. S4 Energy barriers for FE transition of -8.2% strained Gd_2CO_2.

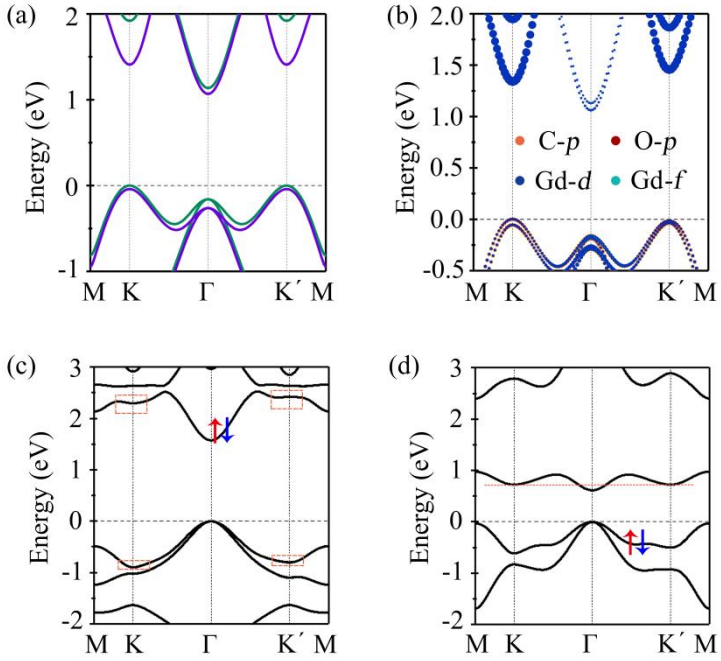

Fig. S5 (a) Band structures of SL Gd_2CO_2 without SOC. Purple and green lines represent spin-up and spin-down channels, respectively. (b) Orbital-resolved band structures of SL Gd_2CO_2 with SOC. Band structures of SL Gd_2CO_2 under state-PE (c) without and (d) with strain. The Fermi level is set to 0 eV.

Fig. S1(b) shows the phonon spectra of the strained Gd_2CO_2, from which we can see slight imaginary frequencies around the Γ point, indicating its stability. For -8.2% strained Gd_2CO_2 with nAFM ground state, the local magnetic moments on Gd_A and Gd_B under state-I (state-II) state are obtained to be -7.039 (-7.062) and 7.062 (7.039) μ_B, implying nonequivalent sublattices and the existence of a net magnetic moment. The net magnetic moment under state-I (state-II) is 0.038 (-

0.038) μ_B per unit cell. The calculated electric polarization is 12.76 (-12.76) pC/m for state-I (state-II), respectively. The FE switching barrier is 0.57 eV/f.u. (**Fig. S4**), which is only slightly larger than that of unstressed one, suggesting the feasibility of FE switching. The corresponding band structures with SOC are shown in **Fig. S6(a,b,c,d)**. Clearly, there is a pairs of valleys located at the K and K′ points in the bottom conduction band, and the valley polarization of 66.3 meV occurs spontaneously. As shown in **Fig. S6(a,c)**, the valley of state-I in the conduction band is mainly from the spin-down channel of Gd_A. When transforming into state-II through the atypical breathing of the trigons, the valley of state-II in the conduction band is contributed by the spin-up channel of Gd_B [**Fig. S6(b,d)**]. The calculated Berry curvatures are shown in **Fig. S6(e)**. For state-I (state-II), the Berry curvature at the K valley has a significantly large negative (positive) value. Due to the large Berry curvature, the Bloch carriers at the valleys will acquire an anomalous transverse velocity in the presence of an in-plane electric field and transversely move to one boundary of the system. For example, as illustrated in **Fig. S6(f)**, for state-I (state-II), by shifting the Fermi level between K and K′ valleys in the bottom conduction band, the spin-down (spin-up) electrons in the K valley would accumulate at the right (left) boundary of the sample. Obviously, this gives rise to the ferroelectrically reversible AVH effect, which is driven by the atypical breathing of the trigons.

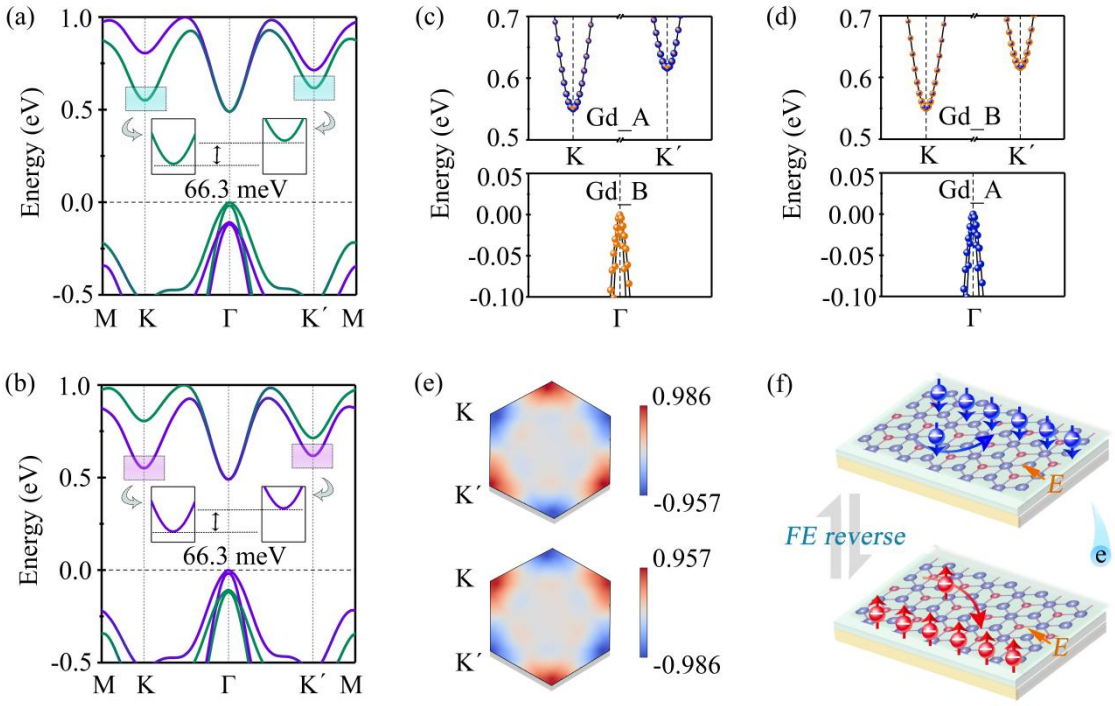

Fig. S6 Spin-resolved band structures of -8.2% strained Gd_2CO_2 under (a) state-I and (b) state-II.

Purple and green lines represent spin-up and spin-down channels, respectively. The Fermi level is set to 0 eV. Sublattice-resolved band structures of (c) state-I and (d) state-II. (e) Berry curvatures for state-I (up panel) and state-II (low panel). (f) Illustrations of ferroelectrically reversible AVH effect.